NANO · MICRO small
www.small-journal.com

Reversible Polymorphic Transition and Hysteresis-Driven Phase Selectivity in Single-Crystalline C8-BTBT Rods

Min-Woo Kim, Sooncheol Kwon, Jehan Kim, Changhoon Lee, Ina Park, Ji Hoon Shim, Il-Seok Jeong, Yong-Ryun Jo, Byoungwook Park, Joo-Hyung Lee, Kwanghee Lee, and Bong-Joong Kim**

Organic semiconductors (OSCs) are highly susceptible to the formation of metastable polymorphs that are often transformed by external stimuli. However, thermally reversible transformations in OSCs with stability have not been achieved due to weak van der Waals forces, and poor phase homogeneity and crystallinity. Here, a polymorph of a single crystalline 2,7-dioctyl[1] benzothieno[3,2-b][1]benzothio-phene rod on a low molecular weight poly(methyl methacrylate) (≈120k) that limits crystal coarsening during solvent vapor annealing is fabricated. Molecules in the polymorph lie down slightly toward the substrate compared to the equilibrium state, inducing an order of greater resistivity. During thermal cycling, the polymorph exhibits a reversible change in resistivity by 5.5 orders with hysteresis; this transition is stable toward bias and thermal cycling. Remarkably, varying cycling temperatures leads to diverse resistivities near room temperature, important for nonvolatile multivalue memories. These trends persist in the carrier mobility and on/off ratio of the polymorph field-effect transistor. A combination of in situ grazing incident wide angle X-ray scattering analyses, visualization for electronic and structural analysis simulations, and density functional theory calculations reveals that molecular tilt governs the charge transport characteristics; the polymorph transforms as molecules tilt, and thereby, only a homogeneous single-crystalline phase appears at each temperature.

1. Introduction

Solution-processed organic semiconductors (OSCs) consisting of π-conjugated molecules have attracted considerable interest due to their wide range of applications, such as biochemical sensors, radio-frequency identification tags, smartphone displays, flexible light sources, portable solar cells, and curved television screens,[1–10] by virtue of their chemical versatility, solution processability, and mechanical flexibility. Charge transport in OSCs is highly sensitive to intermolecular π-orbital overlap, which is directly influenced by deviation in the molecular packing arrangements and/or conformations in crystal lattices. This type of deviation is termed a polymorphism and offers an avenue to optimize device performance-based solely on structural parameters without changing the chemical structures.

Methods to control the polymorphs of OSCs typically exploit templating,[11] solvent selection,[12] crystallization kinetics control,[13] thin film confinement,[14] post-deposition control[15] with others including pressure-induced,[16] mechanically triggered,[17] flow-assisted,[18] vapor-sublimed in air,[19] and light-induced polymorph formation and transition.[20] Despite such efforts, only a few OSCs[12,19] have been subjected to detailed examinations for structure–property relationships of their polymorphs due to difficulties in i) synthesizing individual pure single crystalline phases that eliminate the problems that arise from various grain structures and their grain boundaries, and ii) stabilizing their polymorphs which commonly have similar cohesive energies and low kinetic barriers to solid–solid transformation due to nonselective van der Waals forces and electrostatic interactions.

M.-W. Kim, I.-S. Jeong, Y.-R. Jo, B. Park, J.-H. Lee, Prof. K. Lee, Prof. B.-J. Kim
School of Materials Science and Engineering (SMSE)
Gwangju Institute of Science and Technology (GIST)
Gwangju 61005, Republic of Korea
E-mail: klee@gist.ac.kr; kimbj@gist.ac.kr

The ORCID identification number(s) for the author(s) of this article can be found under https://doi.org/10.1002/smll.201906109.

DOI: 10.1002/smll.201906109

Dr. S. Kwon, Prof. K. Lee
Research Institute for Solar and Sustainable Energies (RISE)
Gwangju Institute of Science and Technology (GIST)
Gwangju 61005, Republic of Korea

Dr. S. Kwon, Prof. K. Lee
Heeger Center for Advanced Materials (HCAM)
Gwangju Institute of Science and Technology (GIST)
Gwangju 61005, Republic of Korea

Dr. J. Kim
Pohang Accelerator Laboratory (PAL)
Pohang University of Science and Technology (POSTECH)
Pohang 790-784, Republic of Korea

Dr. C. Lee, I. Park, Prof. J. H. Shim
Department of Chemistry
Pohang University of Science and Technology (POSTECH)
Pohang 790-784, Republic of Korea

Thermal analysis is one of the most important characterization techniques for understanding the stability relationships between polymorphs. Single-crystal to single-crystal transformation (SCSCT)[21] via thermal treatment has received considerable attention with regard to solid-state reactions and crystal engineering.[22] However, thermally reversible SCSCTs in OSCs, which are essential for reproducible performance and expanded functionality in electronic devices have not been reported up to now, though a few instances of such a property are encountered in some inorganic materials including VO_2[23] and $Ge_2Sb_2Te_5$,[24] and chiral azobenzene crystals,[25] all of which undergo phase transitions between two polymorphs. Additionally, comprehensive studies for clarifying structure–property connections in thermally reversible polymorphism for non-OSCs have not been explored through qualified structural analyses and real device characterizations.[21]

Here, we devise a new method to create a metastable polymorph using the poly(methyl methacrylate) (PMMAs) with low molecular weights (M_{ws}) (i.e., 120k) via solvent vapor annealing (SVA). Surprisingly, the two and three terminal devices with this polymorph present abrupt transitions in resistivity, carrier mobility, and on/off ratio with reversibility and hysteresis. The hysteresis allows us to manipulate the resistivity at room temperature, suggesting the possibility to produce nonvolatile multilevel phase-change memories based on solution-processed organic materials. These devices are also highly stable to a wide range of biases and numerous thermal cycles. We unveil the origin of the transitions in the charge transport properties by exploiting in situ grazing incident wide angle X-ray scattering (GIWAXS), in situ transmission electron microscopy (TEM) measurements, visualization for electronic and structural analysis (VESTA) simulations, and density functional theory (DFT) calculations; the molecular conformation plays a pivotal role without structural and chemical modifications. Such a conformational polymorphism with homogeneous phase transitions assures reliable and reproducible electrical device performance in OSCs.

2. Results and Discussion

To understand the growth properties and related phases of 2,7-dioctyl[1] benzothieno[3,2-b][1]benzothio-phene (C8-BTBT) rods grown on PMMA with a molecular weight (M_w) ranging from 15k to 996k, polarized optical microscopy (POM) images were taken after 30 min of the SVA process as shown in **Figure 1**a–d (see the Experimental Section for detailed growth processes). We find that the length, height, and width of the rods increase with the M_w of PMMA (Figure 1e–g), while the number of the rods decreases (Inset of Figure 1f). Notably, the lengths and widths of the rods were measured at the location of Figure 1a–d and four other locations, whereas the data for the heights were acquired from atomic force microscopy (AFM) images in five areas whose sizes are identical to those of Figure 1a–d. We interpret that such trends could be attributed to the decreasing polarity of the PMMA with increasing M_w, allowing the C8-BTBT molecules to move in an increasingly more active manner on the surface of the PMMA film to form extended dimensions of the rods predominantly via coarsening of the nearby rods[26,27] (see Figure S1 for in situ observation of the growth of the rods, Supporting Information).

To examine the molecular packing structure, selective area electron diffraction (SAED) patterns (see Figure 1i for a representative pattern) were acquired using TEM from the individual rods in four samples grown on PMMAs with different M_{ws} as shown in Figure 1a–d (Supporting Information), revealing that the rods are single crystalline with identical diffraction patterns at [001] zone axis. We further probed the molecular structure of the rod using GIWAXS (Figure 1j; and Figure S2, Supporting Information). The Bragg peaks obtained from the rods grown on PMMAs with four different M_{ws} commonly possess (00L), (20L), (11L), (02L), and (120) observed at $q_{x,y}$ (Å^{-1}) = 0.77, 1.33, and 1.62 and 1.81, respectively. However, the rods on the PMMAs with lower (i.e., 15k and 120k) M_{ws} involve only (122) at $q_{x,y}$ (Å^{-1}) = 1.81, whereas those on the PMMAs with higher M_{ws} (i.e., 350k and 996k) contain both (122) and (121) at the same $q_{x,y}$. The latter indicates the typical monoclinic crystal structure of C8-BTBT in the equilibrium state (space group P21a), while the former on the PMMAs with lower M_{ws} (i.e., 15k and 120k) indicates a metastable polymorph, which is discussed below. Finally, X-ray photoelectron spectroscopy measurements were performed (see Figure S3 for C and S spectra where C1s and S2p peaks shift to lower binding energy with increasing PMMA M_w, Supporting Information). The atomic ratios for the C/S decrease with decreasing PMMA M_w as shown in Figure 1h, implying that C8-BTBT molecules lie down toward the substrate, as presented in the schematics shown in Figure 1h.[28] Therefore, we presume that the formation of the polymorph is associated with molecular conformation (i.e., molecular tilt) in unit cells.

Thermal analyses of the two-terminal devices fabricated with the individual C8-BTBT rods shown in Figure 1 were conducted to examine their intrinsic electrical properties. We prepared two devices with rods grown with 996k and 120k PMMA on SiO_2 substrates as representatives of equilibrium and metastable phases, respectively. The device with the equilibrium phase shows a constant resistivity (ρ) of 2×10^8 Ω cm during thermal cycling between 274 and 317 K (**Figure 2**a). However, the device with the metastable phase demonstrates an intriguing reversible temperature-dependence of resistivity with a hysteresis (see the blue and red data in Figure 2b). During cooling, the resistivity slowly decreases from 2×10^9 Ω cm to 1×10^9 Ω cm (regime I)—a range of resistivities nearly an order higher than that of the equilibrium phase, followed by an abrupt decrease by nearly 4 orders of magnitude down to 1×10^5 Ω cm at 282 K (regime II). Further cooling to 277 K merely doubles the resistivity (regime III). During heating, the resistivity decreases again by a factor of 40 to 5.8×10^3 Ω cm from 277–293 K, (regime IV). Subsequently, the resistivity rapidly increases by ≈5.5 orders, thus showing a full recovery (regime V). Further heating drives an identical behavior of the resistivity to regime I (regime VI). We note that such electrical measurements during thermal cycling were repeated over a wide range of voltages (i.e., ± 0.01 ≈ ± 20 V) and at 0.01 V for 100 instances, which provide data consistent with the ρ versus T plot in Figure 2b (the deviation in the data is ≈ ± 10%) (Figure S4, Supporting Information) while maintaining ohmic conductions (Figure S5, Supporting Information), indicating that the devices with the rods are highly stable to bias and thermal cycling without

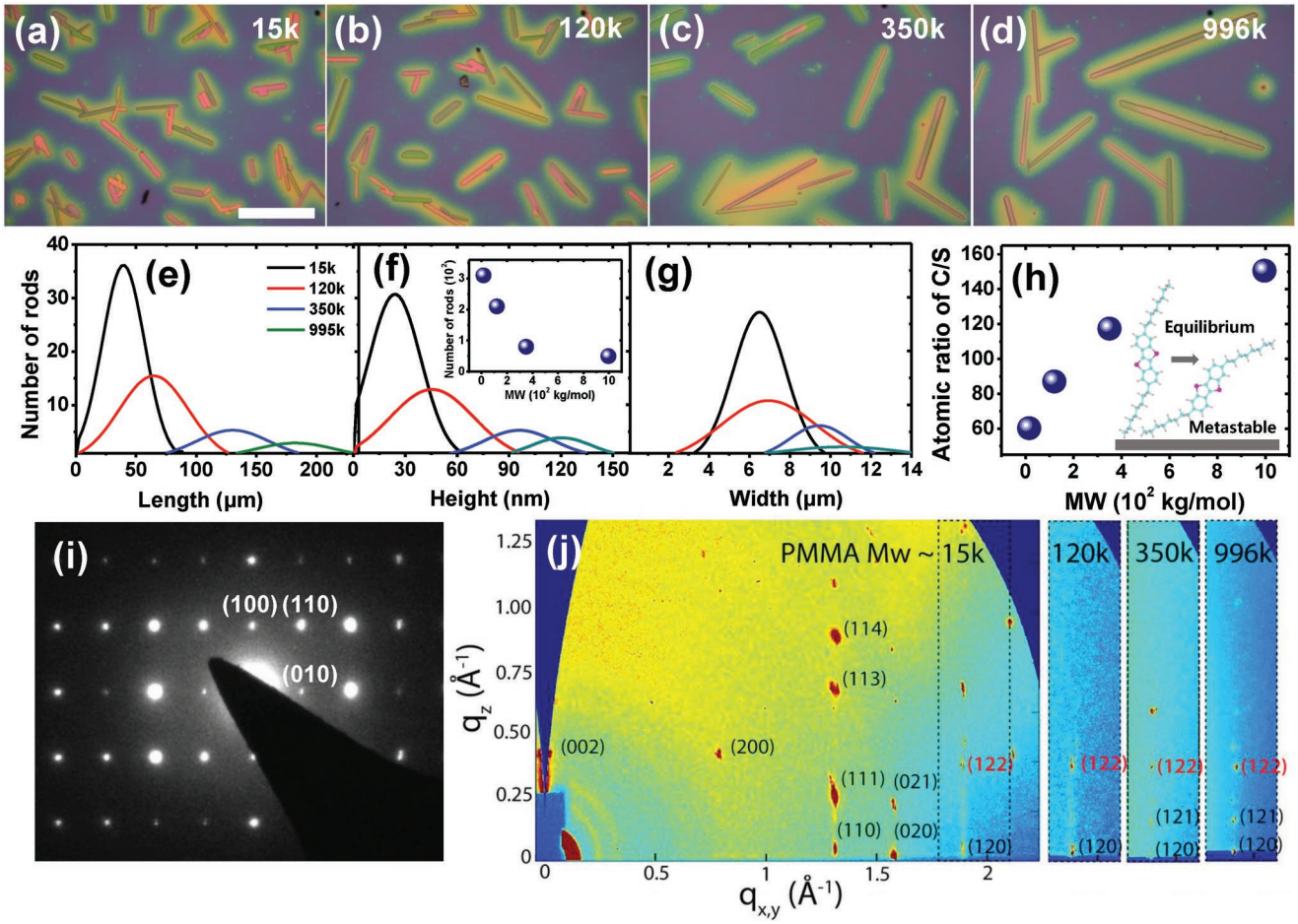

Figure 1. Formation and characterization of a metastable polymorph of C8-BTBT rods. a–d) POM images of C8-BTBT rods grown on PMMAs with various M_{ws}. e–g) Distributions of the length, height, and width of the rods shown in (a–d) and a plot of the number of rods versus M_w in the inset of (f). The scale bar is 100 μm. h) Atomic ratio of C/S as a function of M_w and a schematic depicting the molecular conformations of the equilibrium and metastable phases of the C8-BTBT rods. i) An SAED pattern of a representative C8-BTBT rod shown in (a–d). j) 2D GIWAXS patterns of individual C8-BTBT rods which form in the samples of the PMMAs with four different M_{ws}. The patterns are presented with an emphasis on the (12L) planes.

creating a considerable amount of defects (trap sites) in the crystals. Additionally, we find that capacitance density remains nearly constant and dielectric loss is maintained at ≈3×10^{-2} at 1 MHz during thermal cycling (Figure S6, Supporting Information).

The thermal behavior of the single crystal metastable polymorph of the C8-BTBT rod was also tested using a field-effect transistor (FET) configuration as schematically described in the inset of Figure 2e. Details of the FET structure and its basic properties are illustrated in the Experimental Section and Figure S7 (Supporting Information). The source–drain current ($-I_{ds}$) versus gate–source voltage (V_{gs}) plots obtained during thermal cycling are shown in Figure 2c,d, demonstrating clear evidence of large changes in I_{ds} of 3–4 orders (i.e., 1.7×10^{-13} A ≈ 0.78×10^{-10} A for cooling and 2×10^{-13} A ≈ 1×10^{-9} A for heating) at a narrow range of temperatures (i.e., ≈10 K) with a slight temperature dependence in I_{ds} at the regimes in both extremes. This behavior is induced by the temperature-dependent change in resistivity of the C8-BTBT rod as shown in Figure 2b, irrelevant to gate-induced-drain leakage in the device. We note that the low operational voltages (i.e.,$|V_{gs}| \leq 0.5$ V) used for the measurements arise from the high dielectric constant of the polyvinyl alcohol (PVA) dielectric layer ($\varepsilon \approx 8$).[29] Using these results, saturation regime hole mobilities (μ_h) are acquired and their trends are compared with the ρ versus T plot in Figure 2b,e. During cooling, the initial mobility (1.7×10^{-3} cm^2 V^{-1} s^{-1}) gradually increases to 7.1×10^{-3} cm^2 V^{-1} s^{-1} (regime I), followed by a sudden rise by 2.8 orders to 7.5 cm^2 V^{-1} s^{-1} (regime II). Then, the mobility slightly decreases by ≈37%. During heating, the mobility further increases to 15.6 cm^2 V^{-1} s^{-1} (regime IV). Afterward, the mobility decreases by 3.7 orders (regime V) followed by a slow decrease (regime VI), returning to the initial value of the mobility. This characteristic of the mobility is reasonable due to the inverse dependence with resistivity.[30] Next, the on/off ratio of this FET was observed to show the similar trend with mobility (Figure 2f); the ratio rapidly increases and decreases by about an order within 0.2 V_{gs} during cooling and heating cycles, respectively. The ratio is an order higher compared to the value reported previously.[27] Interestingly, the threshold voltage (V_{th}) is observed to be nearly temperature-independent during thermal cycling (deviation of ≈0.2 V) (see Figure 2e and the fitting curves in Figure S8, Supporting Information), suggesting

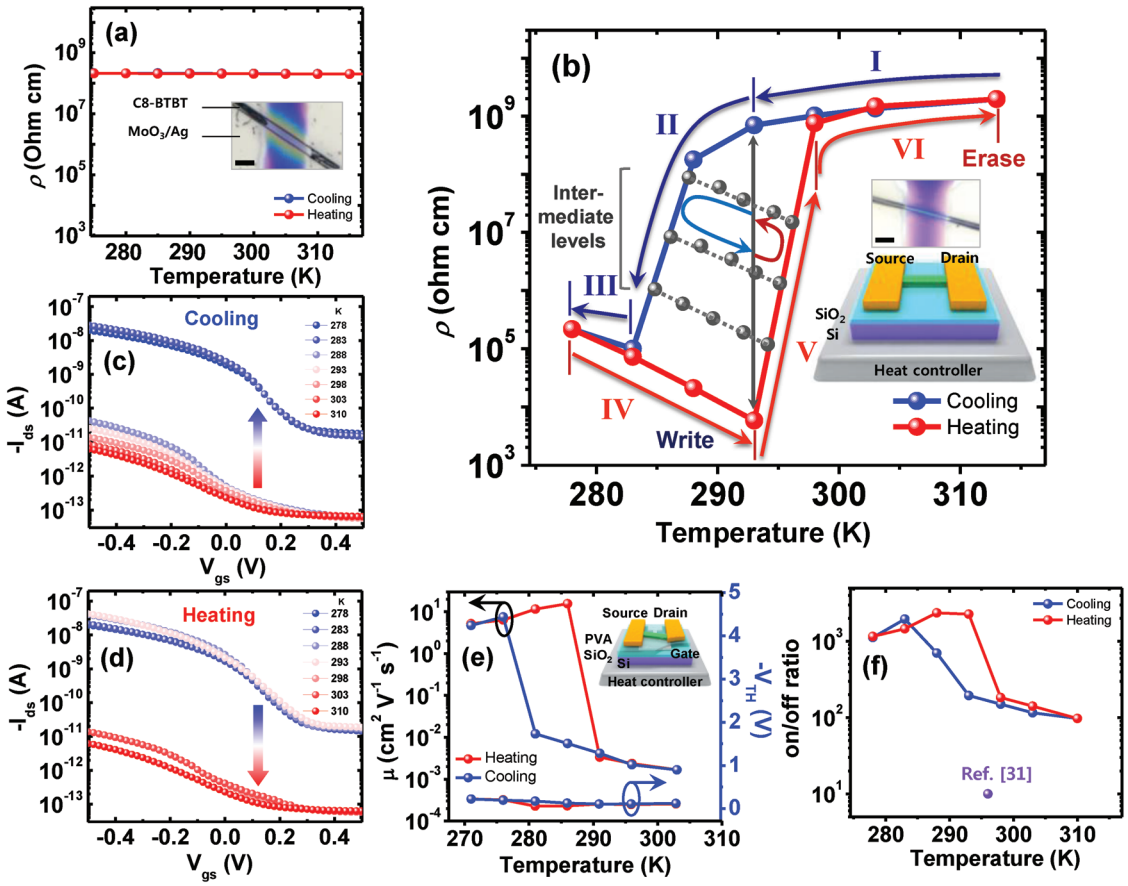

Figure 2. Characterization of the charge transport properties of C8-BTBT polymorphs during thermal cycling. a,b) Temperature dependence of electrical resistivity of the two terminal devices built using the C8-BTBT polymorphs grown on 996k and 120k PMMA, respectively. The POM images in the insets of Figure 1a,b show the two-terminal devices at plan-view, while the schematic in Figure 1b describes the device architecture. The scale bars are 10 µm. The gray vertical line in (b) indicates a room temperature. c,d) I_{ds} versus V_{gs} plots during thermal cycling. e) Hall mobility (μ_h) and threshold voltage (V_{th}) as a function of temperature with an inset depicting the FET structure. f) On/off ratio versus temperature plot compared with the data from ref. [31].

that the localized electronic states at traps and the change in interface conditions are negligible with varying temperature.

To clarify the molecular crystal structure and conformation of the metastable polymorph during thermal cycling, in situ GIWAXS measurements were performed as shown in **Figure 3**a. The data show the diffraction peaks in a specific reciprocal space region for (12L) planes, which help us understand the formation mechanism of the polymorphs (see Figure S9, Supporting Information for the 2D maps for diffraction peaks and **Figure 4**b,c for the 3D maps of diffraction peaks during thermal cycling). We identify that the intensity and position of the diffraction peaks of the (00L), (20L), (11L), (02L) families and (120) remain constant for the entire range of temperatures, indicating that the crystal structure (space group P21a) remains unchanged (see Figure S9, Supporting Information). This result is also supported by the SAED obtained from in situ TEM, revealing that the diffraction pattern is maintained during thermal cycling (see Figure S10 for SAED taken at 260 K, Supporting Information). However, during cooling, the intensity of (122) peak gradually decreases, while a new diffraction peak of (121) begins to appear at 295 K followed by a progressive increase in its intensity. During subsequent heating, the (121) peak intensity decreases with complete disappearance observed at 300 K, while a (122) diffraction peak emerges at 300 K, which gradually increases in intensity up to 317 K. Interestingly, the alternating presence of the two peaks takes place at temperatures that are virtually identical to those at which the resistivity abruptly changes, as shown in the ρ versus T plot in Figure 2b, implying that the maximum and minimum resistivities are attributed to the polymorphs associated with the (122) and (121) peaks, respectively. Notably, a weak diffraction spot, (121)* at q_z (Å^{-1}) = 0.175 (see the gray arrow), located slightly above the (121) peak temporally appears, while the (121) peak dominates the diffraction (i.e., 260–295 K). We speculate that this additional diffraction spot arises from the extra molecular tilt at the interface between the C8-BTBT molecules and the PMMA layer, as indicated by the weak diffraction spot, (002)* at q_z (Å^{-1}) = 0.392 (weaker than the main diffraction spot by a factor of 40), positioned slightly above (002) peak (Figure S11, Supporting Information).

To interpret such a unique polymorphism, we propose that displacement and conformational transition (i.e., tilt) of the molecules play a key role in determining polymorphs occurring during thermal cycling, as illustrated in Figure 3g. We test this scenario using a software, VESTA, which allows us to simulate the diffraction properties of single crystalline molecular structures.[31]

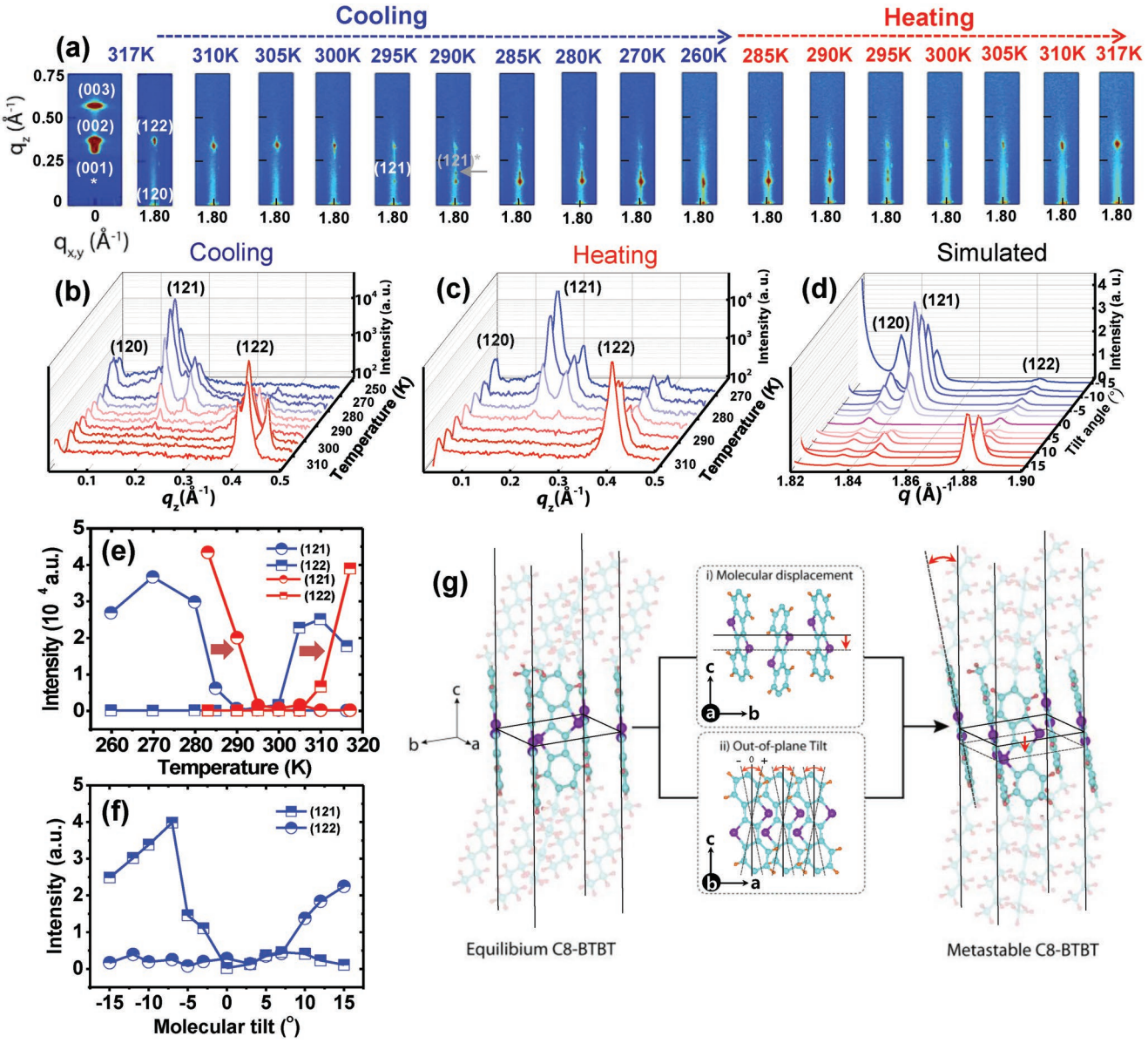

Figure 3. Probing the conformational polymorphism of a metastable C8-BTBT rod via in situ GIWAXS measurements and structural simulations. a) A series of 2D GIWAXS patterns of the (12L) planes of the metastable C8-BTBT polymorph grown on 120k PMMA, which were recorded while cycling the temperature. b,c) 3D GIWAXS maps of a metastable C8-BTBT rod during initial cooling and subsequent heating, respectively. d) Simulated X-ray diffraction patterns of metastable C8-BTBT polymorphs at a molecular displacement (D) of 1.528 Å and at a molecular tilt (θ_a) of $-15° \approx 15°$, obtained using VESTA. e) Intensity profiles of the in situ GIWAXS data shown in (a). f) Intensity profiles of the simulation data shown in (b). g) Schematics illustrating the mechanism by which metastable C8-BTBT polymorphs form.

For this test, we first construct the unit cells where the molecules at the center of the basal planes, (001) are displaced downward along the c-axis, while the molecules at the corners of the unit cell stay in the same places. Notably, the molecules at the two locations have different conformations (i.e., rotated angles), as depicted in the inset of Figure 4a (see the crystal information files (CIFs)), and the lattice parameters of the equilibrium unit cell of C8-BTBT are consistently used for the CIFs of the metastable phases, as confirmed by the GIWAXS data. Figure S12 (Supporting Information) presents the important (120), (121), and (122) diffraction peaks simulated from the unit cells where the molecules at the center of the basal planes are progressively displaced down to 3.056 Å, (0–10% of the unit cell height), revealing that the intensities of the (121) and (122) peaks are significant over the entire range of displacement and for displacements larger than 1.528 Å, an additional strong peak appears at $q_{x,y}$ (Å^{-1}) = 1.842. Such a disagreement with experiments is also observed when tilting molecules to a- and b-axes (i.e., [100] and [010]) by angles of θ_a and θ_b, with respect to the C8-BTBT molecules in an equilibrium state, as the intensities of the (121) and (122) peaks are nearly absent for $-50° \leq \theta_a \leq 50°$ and $-35° \leq \theta_b \leq 35°$ (Figure S13, Supporting

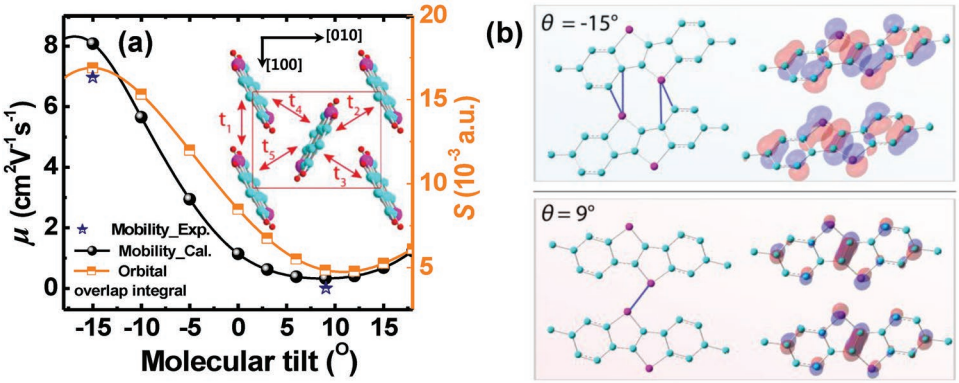

Figure 4. DFT calculations for the charge transport properties of metastable C8-BTBT polymorphs. a) The calculated hole mobility, μ_h, and orbital integral as a function of molecular tilt (θ_a) ranging from 15° to −15°. The inset shows a perspective view of the five possible charge transfer pathways in the C8-BTBT polymorphs. b) Dimer molecular structure and the calculated HOMO (B3LYP/6-31G* level) associated with path t_1 at θ_a = 15° (upper panel) and 9° (lower panel). The cyan and pink circles represent C and S atoms, respectively. The blue solid lines refer to the channels where orbitals interact. For simplicity, BTBT aromatic rings without side chain groups are shown.

Information). Therefore, either displacing or tilting molecules does not adequately describe the polymorphism observed in our experiments.

However, when the molecular displacement is combined with the molecular tilt, we observe that the intensities of the (121) and (122) peaks become strong in turn as the other nearly disappears (3d,f; and Figure S14, Supporting Information). Specifically, a strong (122) peak appears at displacement (D) = 1.528 Å (5% of the unit cell height) and tilt angle to a-axis (θ_a) = 15° (the direction where the current is applied into the devices in Figure 2), and the intensity of the peak diminishes with decreasing θ_a, followed by a near complete vanishment at 5°. A further decrease in θ_a creates the (121) peak, and the intensity of the peak becomes maximized when θ_a < –7°. This trend in diffraction properties coincides with our experimental results as compared with the intensity versus T plots of the GIWAXS data in Figure 3a–c (the blue data in Figure 3e) allowing us to determine the molecular tilt angle at each temperature. We note that other possibilities of combining the displacement and the tilt angle of molecules do not reproduce the GIWAXS data (Figures S15 and S16, Supporting Information); if the displacement is smaller than the optimum condition, the (122) peak is dominant over the (121) peak for the entire range of tilt angles (Figure S15, Supporting Information), and if it is opposite, an extra peak appears at q_z slightly smaller than the (121) peak, along with the two main peaks (Figure S16, Supporting Information).

To understand the strong temperature dependence of mobility of the metastable polymorphs, we calculate the μ_h of the polymorphs as θ_a varies from 15° to –15° at a given constant D of 1.528 Å using a semiclassical Marcus charge transfer theory[32] and the DFT.[33] The possible charge transport pathways $t_1 \approx t_5$ on (001) plane in a unit cell are depicted in the inset of Figure 4a. The μ_h values of the polymorphs are calculated as a function of θ_a, as shown in Figure 4a (black data), and summarized in Table S1a in the Supporting Information, demonstrating that path t_1 directed to [100] is dominant for charge transport, and the contributions from the other paths $t_2 \approx t_5$ are negligible. The highest (8 cm^2 V^{-1} s^{-1}) and lowest (0.3 cm^2 V^{-1} s^{-1}) μ_h values were acquired at θ_a = – 15° and 9°, and at their corresponding temperatures, respectively. Note that the measured μ_h values in Figure 2e (see the stars in Figure 4a) are consistent with the calculated values.

Such a large modulation in μ_h can be understood from the orbital interaction between monomers. The dimerized molecular structures along path t_1 and their highest occupied molecular orbital (HOMO) charge densities (B3LYP/6-31G* level) are presented for θ_a = –15° (upper panel) and 9° (lower panel) in Figure 4b. Because the π–π interactions of C and S atoms are limited by their bond lengths (i.e., the C—C, C—S, and S—S bond lengths are 3.4, 3.5, and 3.8 Å, respectively),[34,35] the intermolecular interaction becomes effective via one S—S channel at θ_a = 9° and four S—C channels at θ_a = –15°, indicating that stronger orbital overlaps occur in the latter case. The orbital shapes and sizes of dimerized HOMOs reflect that the weight of the C- and S-p orbitals at θ_a = –15° is greater than the weight of the p-orbitals of the S-p orbitals at θ_a = 9°. To verify this, we calculated the orbital overlap integral S as a function of θ_a (orange data in Figure 3c), consistent with the behavior of μ_h.

Hence, these simulation results allow us to explain the entire regimes of the transport properties discussed in Figure 2. The transport properties in all regimes except for regime IV are determined by molecular tilt, indicating that new polymorphs continuously evolve as molecules tilt without phase-coexistence during thermal cycling. However, the hysteresis in regime IV emerges due to the delayed recovery of molecular tilt, as observed in the in situ GIWAXS data at the corresponding range of temperatures (see the heating parts in Figure 3a,c,e); the diffraction intensity plots for the (121) and (122) planes are shifted to higher temperatures by ≈10 K as indicated by the arrows in Figure 3e. From the free energy calculation, we find that the delayed recovery is attributed to a high activation energy barrier for the phase transition because the free energy of the polymorph decreases with decreasing temperature (Figure S17, Supporting Information). All of the conductivity, mobility, and on/off ratio in the hysteresis increase exponentially with temperature common trend of the temperature dependence via a hopping mechanism.[36,37] From the mobility data and the Marcus model[32] in which $\mu_h \approx t^2 \exp\left(-\frac{\lambda}{4kT}\right)$, where t is the transfer integral and λ is the reorganization energy, we extract the λ of 0.1 eV and the t of 0.11 eV at 270–285 K, which agree well

with those obtained by the DFT calculation (Table S1b, Supporting Information).

Interestingly, we discover that such a hysteresis takes place even before reaching the temperature for minimum resistivity, as shown in the gray straight lines and the gray spheres (effectively exponentially dependent with temperature) in Figure 2b. Three lines with the data points in gray color form in the hysteresis loop when cooling stops at 281, 279, and 277 K, following which each of the cooling processes returns to heating. If turning back to cooling, the resistivity follows the same track as heating. Using the analysis shown above, we find that the three lines present virtually the same slopes with clearly separated ranges of resistivities, representing similar reorganization energies and diverse transfer integrals. These features of the hystereses propose a new concept for a nonvolatile multivalue memory device operating in a small range of temperatures near room temperature (283–298 K); thermal cycles write and erase the data, and select the intermediate levels at the extremely low voltage of ≈0.01 V (which is a process of "Read"), rather than significantly varying voltages as found in typical memory devices.[38,39] For functionality, both Write and Erase operations, to and from any level, are possible with high accuracy, allowing reliable multibit memory operation. For example, with respect to room temperature (293 K), transferring to higher levels in conductivity requires heating after cooling (blue arrow), whereas the opposite case needs cooling after heating (red arrow). In this conceptual illustration, we show only three intermediate levels; however, the levels can be further extended by taking advantage of the large modulation of the resistivity (≈5.5 orders) and the minimal deviation (≈10%) of the resistivity during transition and repeated cycling (Figure S4c, Supporting Information).

3. Conclusion

Investigation of the new polymorph of single-crystalline C8-BTBT is of fundamental importance for understanding the impact of molecular conformation (i.e., molecular tilt) on the charge transport properties of OSCs and electronic devices based on OSCs. The polymorph undergoes a reversible phase transition with a large variation in resistivity (≈5.5 orders) and a small hysteresis in temperature (≈10 K) during thermal cycling. Varying the cycling temperature permits the selection of a specific phase; hence, distinguished resistivities appear within the hysteresis loop that are located near room temperature. These features may offer an opportunity to develop real nonvolatile multivalue memory devices built using solution-processed organic materials by altering the temperature in the hysteresis, assuming that a microthermoelectric module[40] is attached to the bottom of the device. The electronic levels in the devices could be multiplied by precise temperature control due to the phase homogeneity during thermal cycling, the high device stability, and the large modulation in resistivity, all of which have not been previously observed in inorganic phase change memories.[41,42] We expect that our device can be used for various applications, such as digital cameras, mobile phones, security digital (SD) cards, solid-state drives (SSD), USB flash drives, tablet computers, cybersecurity, etc. Particularly, our organic-based nonvolatile multilevel memory can also be applied for a flexible ultrahigh-density data storage.

4. Experimental Section

Materials and Solution Preparation: High-purity electronic-grade semiconducting C8-BTBT (≈98%) was synthesized by LUMTEC, Taiwan and was used as received. The insulating PMMAs (M_{ws} ≈ 15, 120, 350, 996 kg mol^{-1}) were purchased from Sigma-Aldrich and used as received. To induce an intermolecular interaction between the C8-BTBT and PMMA in solution, 5 mg of PMMA was directly added into 11.2 mg mL^{-1} C8-BTBT solution dissolved in a chlorobenzene solvent (1 wt%). The final weight ratio of the C8-BTBT and the PMMA template in the solution was 1:1. The solutions were subsequently stirred in the dark at room temperature for more than 24 h and were used without further purification.

Growth of C8-BTBT polymorph rods using the SVA process: The prepared solutions were spin-coated (2000 rpm, 1 min) onto Si/SiO_2 substrates that were cleaned in ultrasonic baths of methanol, acetone, and deionized water, respectively, for 7 min each, and were then treated by an O_2 plasma process (50 W, 50 KHz) for 10 min. For SVA, the spin-coated samples were mounted inside the lid of a jar that was filled with a chloroform solvent. Then, the jar was closed using the lid; the distance between the samples and the surface of the chloroform solvent was 0.5 cm. The prepared jar was subsequently stored in the dark at room temperature for more than 1 h to grow the rod-shaped C8-BTBT polymorph crystals.

Characterization of C8-BTBT Rods: For POM measurements, a Zeiss Axioskop 40 equipped with a charge-coupled device camera was used to monitor the growth kinetics of the C8-BTBT rods after the SVA process. The samples were located in between two polarized glass lenses where one polarizer was orientated at 90° relative to the other with a distance of ≈20 µm. The topographic images of the samples were collected by AFM in tapping mode to probe the differences in the height and width of the prepared C8-BTBT rods used in the POM measurement. TEM bright field images of the samples were recorded using a Tecnai G^2 F30 S-Twin microscope operated at an acceleration voltage of 300 kV. The samples were prepared via direct SVA growth of the rods onto SiO_2 TEM grids (TEMwindows, USA), upon which PMMA was first spin-coated. Furthermore, in situ TEM imaging at low temperatures down to 260 K was performed using a double-tilt cooling holder (Gatan, USA).

In situ GIWAXS measurements were performed at the 3C-SAXSl beam line in the Pohang Accelerator Laboratory (PAL) using a monochromatized X-ray radiation source at an energy of 10.55 eV ($\lambda = 0.117$ nm) and a 2D charge-coupled device (CCD) detector (Mar165 CCD). The C8-BTBT rod samples were mounted onto a *z*-axis goniometer equipped with a vacuum chamber (≈10^{-3} Torr) and a Peltier plate, which provided excellent temperature accuracy along with a reliable cooling/heating rate (10 °C min^{-1}). The samples were placed at a distance of 0.201 m away from the CCD detector. The incident angle of each X-ray beam was set as 0.1°, and the scattering angles were determined from the positions of the X-ray beam reflected from the silicon substrate using precalibrated silver behenate.

Device Fabrication and Characterization: Before coating C8-BTBT:PMMA solutions on the substrates, heavily n-type-doped silicon substrates covered with a 200 nm thick SiO_2 layer were sonicated with acetone and isopropyl alcohol, respectively, for 10 min and dried at 100 °C for 15 min. The C8-BTBT:PMMA solutions were deposited onto the substrates at room temperature and ambient conditions followed by the aforementioned SAV process to form C8-BTBT rods. The fabrication of two-terminal devices with the rods was completed by depositing MoO_3/Ag electrodes at both ends of the rod with a channel length and width of ≈20 and ≈10 µm, respectively. For the top-contact and bottom-gate FETs, a 30 nm thick aluminum layer was initially deposited as a gate electrode using a shadow mask on a glass substrate (1.5 × 1.5 cm^2). After spin-casting a 5 wt% PVA aqueous solution mixed with ammonium dichloromate that was deposited onto the prepared substrate, the PVA gate insulator ($\varepsilon \approx 8$) using ultraviolet (UV) light for 90 s was exposed and cross-linked; the final film was rinsed with deionized (DI) water. Then, the polymorphic C8-BTBT rods were grown on the substrate via the SVA process. Next, MoO_3/Ag contact electrodes with channel length (L) ≈20 µm and channel width (W) ≈10 µm were deposited at both ends of the rod. The temperature-dependent resistivity, charge transfer, and

output characteristics were measured in an N_2-filled glove box using a Keithley 4200 source meter (internal impedance > 10^{10} Ω) equipped with a Peltier plate (cooling/heating rate (10 °C 1 min^{-1})). The saturation-regime mobility of the transistor was determined using the following equation: $Ids = (WCi/2L)\ \mu s\ at(Vg - Vth)^2$, where Ids is the source–drain current, Ci (35.1 nF cm^{-2}) is the capacitance per unit area, L is the channel length, W is the channel width, and Vg and Vth are the gate and threshold voltages, respectively.

Theoretical Studies of Simulated C8-BTBT: For the DFT calculations, the Becke's three-parameter hybrid method and the Lee–Yang–Parr correlation functional (B3LYP)[43] with 6-31G* basis sets implemented in the Gaussian 09 package were employed.[44,45] The equilibrium lattice parameters obtained from GIWAXS measurements were used. Vibrational frequencies for evaluating the free energy were calculated using B3LYP/6-31G* with tight criteria for the convergence in energies, forces, and the integral grid. The calculated HOMO contributions at $\theta_a = 15°$ and 9° were visualized using GaussView3.

The mobility of charge carriers is described based on the Einstein relation

$$\mu = \frac{ed^2k}{2k_BT} \tag{1}$$

where e is the electronic charge, d is the distance between molecular centers in a dimer, and $k = (k_{ij})$ is the intermolecular charge transfer rate derived from Marcus theory assuming a semiclassical approximation for the transfer mechanism in the hopping regime

$$k_{ij} = t_{ij}^2\sqrt{\frac{\pi}{\hbar^2 k_B T\lambda_{ij}}}\exp\left[-\frac{\left(\Delta E_{ij} - \lambda_{ij}\right)^2}{4\lambda_{ij}k_BT}\right] \tag{2}$$

Here, λ_{ij} is the reorganization energy, $\Delta E_{ij} = \varepsilon_i - \varepsilon_j$ where ε_i is the energy of site i, and t_{ij} is the transfer integral. To calculate t_{ij}, a direct calculation method adopted from Valeev et al.[46] was used.

Supporting Information

Supporting Information is available from the Wiley Online Library or from the author.

Acknowledgements

M.K., S.K., and J.K. contributed equally to this work. This research was supported by NRF-2017R1A2B4003615, NRF-2018R1C1B6006177, NRF-2017R1D1A1B03036257, NRF-2017K2A9A1A06037859, Samsung Research Funding Center of Samsung Electronics under Project Number SRFC-MA1402-10 and "GIST-Caltech Research Collaboration" grant funded by the GIST in 2019. The authors thank the Heeger Center for Advanced Materials (HCAM) and the Research Institute of Solar and Sustainable Energies (RISE) for assistance with device fabrication and characterization.

Conflict of Interest

The authors declare no conflict of interest.

Keywords

2,7-dioctyl[1] benzothieno[3,2-b][1]benzothio-phene (C8-BTBT), nonvolatile multivalue memory, organic semiconductors, polymorph, single crystal

Received: October 23, 2019
Revised: November 22, 2019
Published online:

[1] *Nat. Mater.* **2013**, *12*, 591.
[2] J. E. Anthony, *Nat. Mater.* **2014**, *13*, 773.
[3] J. A. Rogers, Z. Bao, *J. Polym. Sci., Part A: Polym. Chem.* **2002**, *40*, 3327.
[4] G. H. Gelinck, H. E. A. Huitema, E. van Veenendaal, E. Cantatore, L. Schrijnemakers, J. B. P. H. van der Putten, T. C. T. Geuns, M. Beenhakkers, J. B. Giesbers, B.-H. Huisman, E. J. Meijer, E. M. Benito, F. J. Touwslager, A. W. Marsman, B. J. E. van Rens, D. M. de Leeuw, *Nat. Mater.* **2004**, *3*, 106.
[5] V. Subramanian, J. M. J. Frechet, P. C. Chang, D. C. Huang, J. B. Lee, S. E. Molesa, A. R. Murphy, D. R. Redinger, S. K. Volkman, *Proc. IEEE* **2005**, *93*, 1330.
[6] P. F. Baude, D. A. Ender, M. A. Haase, T. W. Kelley, D. V. Muyres, S. D. Theiss, *Appl. Phys. Lett.* **2003**, *82*, 3964.
[7] T. Someya, A. Dodabalapur, J. Huang, K. C. See, H. E. Katz, *Adv. Mater.* **2010**, *22*, 3799.
[8] D. J. Lipomi, M. Vosgueritchian, B. C.-K. Tee, S. L. Hellstrom, J. A. Lee, C. H. Fox, Z. Bao, *Nat. Nanotechnol.* **2011**, *6*, 788.
[9] S. C. B. Mannsfeld, B. C.-K. Tee, R. M. Stoltenberg, C. V. H.-H. Chen, S. Barman, B. V. O. Muir, A. N. Sokolov, C. Reese, Z. Bao, *Nat. Mater.* **2010**, *9*, 859.
[10] K. Kuribara, H. Wang, N. Uchiyama, K. Fukuda, T. Yokota, U. Zschieschang, C. Jaye, D. Fischer, H. Klauk, T. Yamamoto, K. Takimiya, M. Ikeda, H. Kuwabara, T. Sekitani, Y.-L. Loo, T. Someya, *Nat. Commun.* **2012**, *3*, 723.
[11] A. O. F. Jones, Y. H. Geerts, J. Karpinska, A. R. Kennedy, R. Resel, C. Röthel, C. Ruzié, O. Werzer, M. Sferrazza, *ACS Appl. Mater. Interfaces* **2015**, *7*, 1868.
[12] G. Giri, R. Li, D.-M. Smilgies, E. Q. Li, Y. Diao, K. M. Lenn, M. Chiu, D. W. Lin, R. Allen, J. Reinspach, S. C. B. Mannsfeld, S. T. Thoroddsen, P. Clancy, Z. Bao, A. Amassian, *Nat. Commun.* **2014**, *5*, 3573.
[13] G. Giri, E. Verploegen, S. C. B. Mannsfeld, S. Atahan-Evrenk, D. H. Kim, S. Y. Lee, H. A. Becerril, A. Aspuru-Guzik, M. F. Toney, Z. Bao, *Nature* **2011**, *480*, 504.
[14] Y. Diao, K. M. Lenn, W.-Y. Lee, M. A. Blood-Forsythe, J. Xu, Y. Mao, Y. Kim, J. A. Reinspach, S. Park, A. Aspuru-Guzik, G. Xue, P. Clancy, Z. Bao, S. C. B. Mannsfeld, *J. Am. Chem. Soc.* **2014**, *136*, 17046.
[15] A. M. Hiszpanski, Y.-L. Loo, *Energy Environ. Sci.* **2014**, *7*, 592.
[16] L. Wang, B. Liu, H. Li, W. Yang, Y. Ding, S. V. Sinogeikin, Y. Meng, Z. Liu, X. C. Zeng, W. L. Mao, *Science* **2012**, *337*, 825.
[17] H. Ito, M. Muromoto, S. Kurenuma, S. Ishizaka, N. Kitamura, H. Sato, T. Seki, *Nat. Commun.* **2013**, *4*, 2009.
[18] S.-L. Lee, Z. Yuan, L. Chen, K. S. Mali, K. Müllen, S. De Feyter, *J. Am. Chem. Soc.* **2014**, *136*, 4117.
[19] T. He, M. Stolte, C. Burschka, N. H. Hansen, T. Musiol, D. Kälblein, J. Pflaum, X. Tao, J. Brill, F. Würthner, *Nat. Commun.* **2015**, *6*, 5954.
[20] L. Pithan, C. Cocchi, H. Zschiesche, C. Weber, A. Zykov, S. Bommel, S. J. Leake, P. Schäfer, C. Draxl, S. Kowarik, *Cryst. Growth Des.* **2015**, *15*, 1319.
[21] D. Das, E. Engel, L. J. Barbour, *Chem. Commun.* **2010**, *46*, 1676.
[22] M.-L. Cao, H.-J. Mo, J.-J. Liang, B.-H. Ye, *CrystEngComm* **2009**, *11*, 784.
[23] J. H. Park, J. M. Coy, T. S. Kasirga, C. Huang, Z. Fei, S. Hunter, D. H. Cobden, *Nature* **2013**, *500*, 431.
[24] K. Shportko, S. Kremers, M. Woda, D. Lencer, J. Robertson, M. Wuttig, *Nat. Mater.* **2008**, *7*, 653.
[25] F. Tan, A. López-Periago, M. E. Light, J. Cirera, E. Ruiz, A. Borrás, F. Teixidor, C. Viñas, C. Domingo, J. G. Planas, *Adv. Mater.* **2018**, *30*, 1800726.
[26] C. Liu, T. Minari, Y. Li, A. Kumatani, M. V. Lee, S. H. A. Pan, K. Takimiya, K. Tsukagoshi, *J. Mater. Chem.* **2012**, *22*, 8462.
[27] C. Liu, T. Minari, X. Lu, A. Kumatani, K. Takimiya, K. Tsukagoshi, *Adv. Mater.* **2011**, *23*, 523.

[28] M. Zhu, L. Lyu, D. Niu, H. Zhang, S. Wang, Y. Gao, *RSC Adv.* **2016**, *6*, 112403.
[29] S. Vasimalla, N. V. V. Subbarao, M. Gedda, D. K. Goswami, P. K. Iyer, *ACS Omega* **2017**, *2*, 2552.
[30] R. F. Pierret, *Semiconductor Fundamentals*, Vol. *1*, Addison Wesley, MA **1988**.
[31] F. Izumi, K. Momma, *Solid State Phenom.* **2007**, *130*, 15.
[32] R. A. Marcus, *Rev. Mod. Phys.* **1993**, *65*, 599.
[33] B. Baumeier, J. Kirkpatrick, D. Andrienko, *Phys. Chem. Chem. Phys.* **2010**, *12*, 11103.
[34] V. Coropceanu, J. M. André, M. Malagoli, J. L. Brédas, *Theor. Chem. Acc.* **2003**, *110*, 59.
[35] A. Bondi, *J. Phys. Chem.* **1964**, *68*, 441.
[36] Y. Zhang, J. Qiao, S. Gao, F. Hu, D. He, B. Wu, Z. Yang, B. Xu, Y. Li, Y. Shi, W. Ji, P. Wang, X. Wang, M. Xiao, H. Xu, J.-B. Xu, X. Wang, *Phys. Rev. Lett.* **2016**, *116*, 016602.
[37] I. I. Fishchuk, A. K. Kadashchuk, J. Genoe, M. Ullah, H. Sitter, T. B. Singh, N. S. Sariciftci, H. Bässler, *Phys. Rev. B* **2010**, *81*, 045202.
[38] Y. Ji, D. F. Zeigler, D. S. Lee, H. Choi, A. K.-Y. Jen, H. C. Ko, T.-W. Kim, *Nat. Commun.* **2013**, *4*, 2707.
[39] J. Ouyang, C.-W. Chu, C. R. Szmanda, L. Ma, Y. Yang, *Nat. Mater.* **2004**, *3*, 918.
[40] C. Gould, N. Shammas, *Micro Electronic and Mechanical Systems*, IntechOpen **2009**, https://doi.org/10.5772/7001.
[41] R. E. Simpson, P. Fons, A. V. Kolobov, T. Fukaya, M. Krbal, T. Yagi, J. Tominaga, *Nat. Nanotechnol.* **2011**, *6*, 501.
[42] W. Zhang, R. Mazzarello, M. Wuttig, E. Ma, *Nat. Rev. Mater.* **2019**, *4*, 150.
[43] M. J. Frisch, G. W. Trucks, H. B. Schlegel, G. E. Scuseria, M. A. Robb, J. R. Cheeseman, G. Scalmani, V. Barone, B. Mennucci, G. A. Petersson, H. Nakatsuji, M. Caricato, X. Li, H. P. Hratchian, A. F. Izmaylov, J. Bloino, G. Zheng, J. L. Sonnenberg, M. Hada, M. Ehara, K. Toyota, R. Fukuda, J. Hasegawa, M. Ishida, T. Nakajima, Y. Honda, O. Kitao, H. Nakai, T. Vreven, J. A. Montgomery Jr., J. E. Peralta, F. Ogliaro, M. Bearpark, J. J. Heyd, E. Brothers, K. N. Kudin, V. N. Staroverov, R. Kobayashi, J. Normand, K. Raghavachari, A. Rendell, J. C. Burant, S. S. Iyengar, J. Tomasi, M. Cossi, N. Rega, J. M. Millam, M. Klene, J. E. Knox, J. B. Cross, V. Bakken, C. Adamo, J. Jaramillo, R. Gomperts, R. E. Stratmann, O. Yazyev, A. J. Austin, R. Cammi, C. Pomelli, J. W. Ochterski, R. L. Martin, K. Morokuma, V. G. Zakrzewski, G. A. Voth, P. Salvador, J. J. Dannenberg, S. Dapprich, A. D. Daniels, Ö. Farkas, J. B. Foresman, J. V. Ortiz, J. Cioslowski, D. J. Fox, *Gaussian 09 (Revision A.02)*, Gaussian Inc, Wallingford, CT **2009**.
[44] A. D. Becke, *J. Chem. Phys.* **1993**, *98*, 5648.
[45] C. Lee, W. Yang, R. G. Parr, *Phys. Rev. B* **1988**, *37*, 785.
[46] E. F. Valeev, V. Coropceanu, D. A. da Silva Filho, S. Salman, J.-L. Brédas, *J. Am. Chem. Soc.* **2006**, *128*, 9882.